

The thermodynamics of CaSiO₃ in Earth’s lower mantle

Yongjoong Shin,¹ Enrico Di Lucente,¹ Nicola Marzari,^{1,2} and Lorenzo Monacelli^{3,1}

¹*Theory and Simulation of Materials (THEOS) and National Centre for Computational Design and Discovery of Novel Materials (MARVEL), École Polytechnique Fédérale de Lausanne, Lausanne 1015, Switzerland*

²*Laboratory for Materials Simulations, Paul Scherrer Institut, 5232 Villigen PSI, Switzerland*

³*Dipartimento di Fisica, Università di Roma Sapienza, 00185 Roma, Italy*

The lower mantle of Earth, characterized by pressures of 24-127 GPa and temperatures of 1900-2600 K, is still inaccessible to direct observations. In this work, we investigate by first principles the stability, phase diagram, elastic properties, and thermal conductivity of CaSiO₃, that constitutes a significant component of Earth’s lower mantle. Notably, our simulations capture in full the anharmonic ionic fluctuations arising from the extreme temperatures and pressures of the lower mantle, thanks to the use of stochastic self-consistent harmonic approximation (SSCHA).

We show that the cubic phase of CaSiO₃ is the stable state at the lower mantle’s thermodynamic conditions. The phase boundary between the cubic and tetragonal phases is of first-order and increases linearly from 300 K to 1000 K between 12 GPa and 100 GPa. Accounting for temperature-renormalized phonon dispersions, we evaluate the speed of sound as a function of depth. Our results downplay the role of octahedral rotations on the transverse sound velocity of cubic CaSiO₃, advocated in the past to explain discrepancies between theory and experiments. The lattice thermal conductivity, assessed thanks to the recently introduced Wigner formalism, shows a predominance of particle-like transport, thus justifying the use of the standard Boltzmann transport equation even in a system with such strong ionic anharmonicity.

Despite our proximity to Earth’s lower mantle, the journey to explore it remains far more distant than venturing into the cosmos. The Earth’s lower mantle has a temperature around 2000 K¹ and pressures between 24 to 127 GPa². CaSiO₃ constitutes about 10% of the lower mantle’s mass, and its precise mechanical and thermodynamical characterization under such extreme conditions is still missing. Both experiments and theoretical simulations show that CaSiO₃ exists in the Ca-perovskite structure above 12 GPa³⁻⁶; however, its phase diagram remains mostly unknown. For example, contradictory data have been reported on the crystal symmetry—cubic (Pm $\bar{3}$ m space group) vs tetragonal (I4/mcm space group)—at high pressures and temperatures⁷⁻⁹. Furthermore, seismology of our planet relies on the precise estimation of sound velocities at the relevant thermodynamic conditions¹⁰. However, due to practical challenges in reproducing the high temperature and pressures of lower mantle, most experimental data on the elastic properties of CaSiO₃ have been reported for the tetragonal phase at room temperature¹¹⁻¹⁶. Therefore, the propagation speed of longitudinal and transverse seismic waves as a function of depth, necessary for accurate geological modeling of the Earth’s interior, remains unknown. Last, the prediction of lattice thermal conductivities from first principles is a very active area of research, with the complex phenomenology of phonon-phonon scattering in solids being intensively investigated¹⁷⁻³². In the context of geophysics, the knowledge of thermal conductivity is crucial to determine the planet’s internal dynamics and evolution, specifically at the core-mantle boundary where mass transport is impeded³³.

can reproduce the lower mantle condition *in silico*³⁴. However, the strongly anharmonic fluctuations of ions due to high temperature and large quantum fluctuations of lattice phonons pose significant challenges for standard approaches. Previous studies on CaSiO₃ mainly employed the quasi-harmonic approximation (QHA)^{7,35}, which can describe volume-dependent thermal effects in materials with some degree of anharmonicity. Still, it fails in cubic CaSiO₃, where harmonic phonons are unstable. Various methods have been employed to overcome this issue^{7,12}, the most successful one being first principles molecular dynamics (FPMD)^{8,36}, which shows how the crystal remains tetragonal up to 3000 K but appears cubic when averaged over time. This scenario points toward an order-disorder phase transition, for which determining the phase boundary within FPMD simulations is very demanding.

Also, the computational evaluation of the speed of sound and elastic properties CaSiO₃ presents significant challenges. In fact, the bulk and shear moduli significantly differ between the tetragonal and cubic phases. Thus, it is fundamental to elucidate both the precise phase diagram of the material and the role played by the lattice vibration at several thousands Kelvin³⁷.

The geological modeling of Earth also relies on the determination of heat flows from the Earth’s core to the lower mantle. This process is regulated by the thermal conductivity (κ) of materials composing the core-lower mantle interface³⁸⁻⁴¹, of which CaSiO₃ is one of the major constituents. A recent study reported a systematic calculation of CaSiO₃ thermal conductivity⁴². However, coherent wave-like transport^{17,43} may become relevant at temperatures of several thousands Kelvin, and its role is yet to be investigated.

Computer simulations are thus very precious, as they

In this work, we simulate from first principles the phase diagram, sound velocities, and thermal conductivity of CaSiO_3 between 20-100 GPa and 300-3000 K accounting for the anharmonic and quantum fluctuations of ions. For this purpose, we combine density-functional theory (DFT) at the PBEsol level⁴⁴ with the stochastic self-consistent harmonic approximation (SSCHA)^{45–50}, a method able to compute the thermodynamics properties of solids arising from anharmonic vibrations of the lattice by minimizing the free energy with a Gaussian density matrix ansatz for the ionic degrees of freedom. We calculate the precise phase boundary between the cubic and tetragonal phase of CaSiO_3 , unveiling the origin of the phase transition, and compute its bulk modulus, shear modulus, and thermal conductivity. More details on the computational methodology are provided in the Methods section.

RESULTS

A. Phase diagram and microscopic origin of the phase transition

There are contradictory reports on the origin of the phase transition in CaSiO_3 ^{7–9}. In particular, it is unclear if the transition kind is first-order, order-disorder (similar to BaTiO_3 ^{51,52}), or second-order displacive (as in CsSnI_3 ⁵³). In the order-disorder scenario, the cubic structure with 5 atoms per primitive cell is unstable even at high temperatures; the system reorganizes its lattice within a larger cell, characterized by disordered local displacements that, on average, retain cubic symmetry⁵⁴. In the first-order scenario, the cubic and tetragonal structures can coexist in the same thermodynamic conditions: the transition occurs when the free energy of the two phases is the same. The displacive transition is instead a typical second-order phenomenon where the distortion from the cubic lattice (order parameter) continuously disappears with increasing temperature. The displacive transition is marked by a critical point where the correlation function of the order parameter diverges in the thermodynamic limit; this critical point coincides with the softening of a phonon mode, which approaches zero energy. It is exceptionally challenging for FPMD to disentangle the different mechanisms, as the similarity between the cubic and tetragonal phases prevents a clear identification of the structure from snapshots of the dynamics. Moreover, investigating the existence of the critical point or a disordered cubic structure is cumbersome in finite-size systems, requiring a systematic analysis of the thermodynamic limit through the simulation of cells containing thousands of atoms, often beyond the reach of first-principles calculations.

To elucidate the mechanism underlying the phase transition, we compare the stability of the 5-atoms cubic phase (Figure 1a,c), the evolution of the order parameters in the tetragonal phase (Figure 1b), and the free energy

differences between cubic and tetragonal structures (Figure 1d). We run the simulations at 0 GPa, 50 GPa, and 100 GPa (see also SI. 1 in supplementary information), reporting a detailed analysis in Figure 1 only for the latter pressure. The (meta)stability of a structure can be identified from the sign of the anharmonic free energy Hessian eigenvalues⁴⁶

$$\frac{1}{\sqrt{m_i m_j}} \frac{\partial^2 F}{\partial \mathcal{R}_{i\alpha} \partial \mathcal{R}_{j\beta}} = \sum_{\mu} e_{\mu i\alpha} e_{\mu j\beta} \omega_{\mu}^2. \quad (1)$$

Here, ω_{μ} and e_{μ} define the μ -th static anharmonic phonon frequency and the respective polarization vector; m_i is the mass of the i -th atom; the i, j indicate the atomic indices while α, β the Cartesian coordinates. If ω_{μ} is imaginary, the Hessian of the free energy is not positive definite, and the structure is unstable. At 100 GPa, the 5-atoms cubic phase is stable above 300 K (the temperature at which the imaginary phonon at R disappears in Figure 1a and c). Interestingly, even at 0 K, anharmonic phonon dispersions deviate from the harmonic calculations, emphasizing the importance of anharmonicity even when ions fluctuate only due to quantum zero-point motion, included within the SSCHA⁴⁸. Increasing the temperature, the rotations of the oxygen octahedra energy (the M-R unstable modes) stiffen. Instead, high-energy phonon bands, representing the expansion and contraction of the oxygen cage, become softer upon heating. Since a temperature above 1000 K is necessary to populate high-energy modes, their redshift at lower temperatures indicates their coupling with a low-energy phonon band. By selectively inhibiting scattering with low-frequency modes in the calculation of the free energy Hessian (see Methods section), we determine that the significant phonon-phonon interactions of the high-energy bands occurs with the rattling of the calcium atoms. On the opposite, the rotational modes of oxygen octahedra that trigger the phase transition do not interact with high energy bands.

While the simulation of the free energy Hessian shows that a temperature of 400 K is enough to remove the instabilities of the cubic phase at 100 GPa, the free energy of the tetragonal phase remains lower than the cubic one until 800 K (Figure 1d). This rules out the second-order displacive phase transition hypothesis: the tetragonal phase has a lower free energy at the critical point where the cubic phase stabilizes. In Figure 1b we report the order parameter, defined as the difference between the average positions of atoms and the Wyckoff positions of the Pm3m cubic phase, as a function of temperature. An abrupt transition into the cubic phase occurs at 800 K. This is consistent with a first-order scenario, where the cubic and tetragonal phases can coexist in a wide range of temperatures between 400 K and 800 K. Thanks to the determination of the free energy difference (Figure 1d), we identify the transition temperature at 800 K (100 GPa). Taking into account also our simulations at 0 GPa and 50 GPa, we show the resulting phase diagram of CaSiO_3 in Figure 2. Our calculations

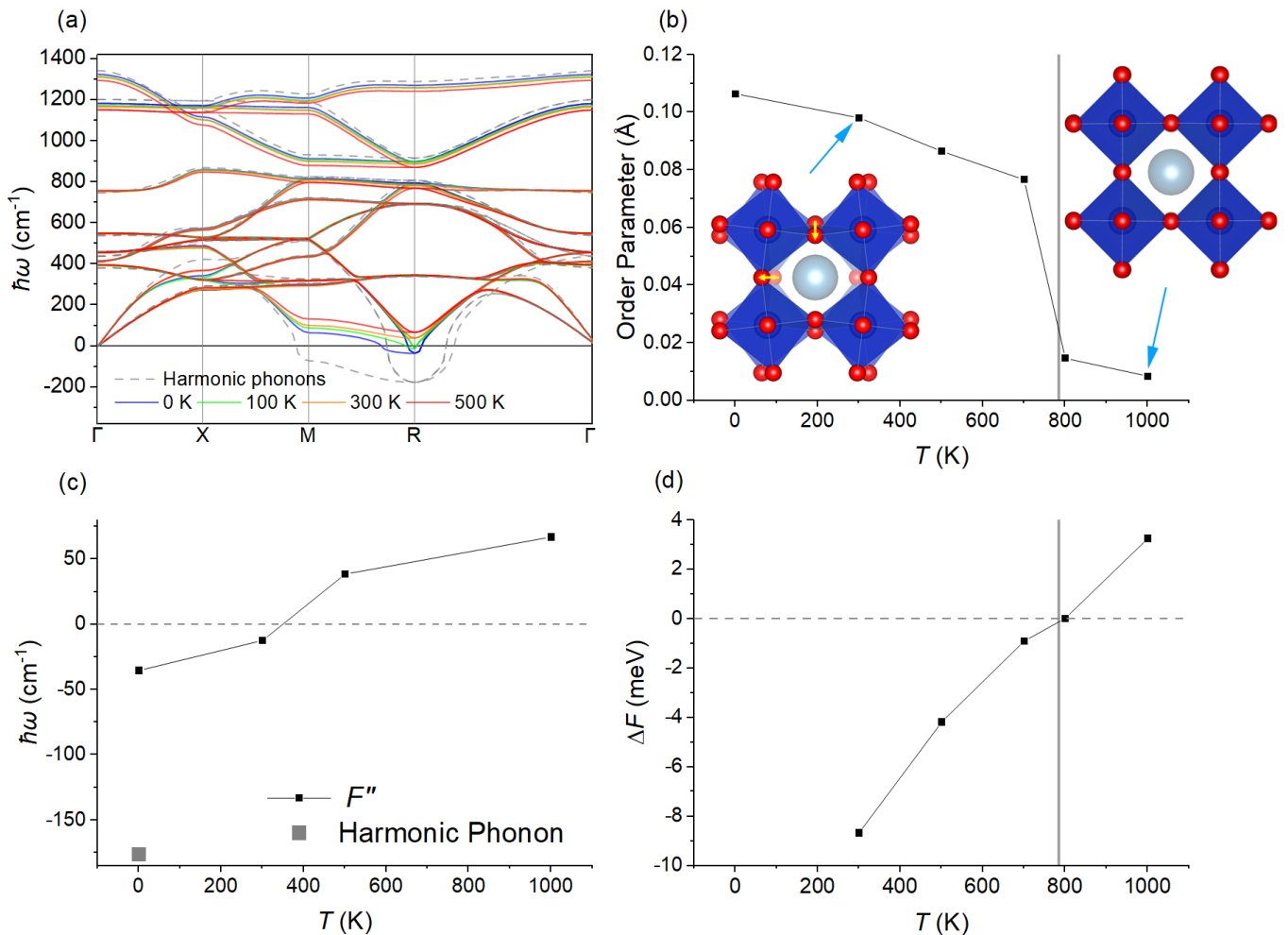


Figure 1: Phase stability for CaSiO₃ at 100 GPa, across the transition from the cubic $Pm\bar{3}m$ to the tetragonal $I4/mcm$ structure. (a) Anharmonic phonons in cubic CaSiO₃ as a function of temperature (obtained as the square root eigenvalues of the free energy landscape Hessian matrix). Dashed lines indicate the harmonic dispersion computed within density-functional perturbation theory (DFPT). The 0 K dispersions do not match with DFPT, as it also accounts for anharmonicity induced by finite fluctuations of ions due to quantum zero-point motion. (b) Order parameter as a function of temperature: the order parameter is chosen as the difference between the average positions of atoms and the Wyckoff positions of the high-symmetry cubic phase. We also show the crystal average structure at 300 K and 1000 K (before and after the transition). (c) The lowest frequency of the free energy Hessian $F'' = \frac{\partial^2 F}{\partial R_a \partial R_b}$ at the R point as a function of temperature. Negative (imaginary) values indicate instability. (d) Free energy difference between the cubic and tetragonal phases as a function of temperature; the vertical line identifies the phase transition.

agree perfectly with available experimental elastic X-ray diffraction data¹² and underline how the cubic $Pm\bar{3}m$ phase is stable already at relatively low temperatures and is the dominant phase of CaSiO₃ in Earth's lower mantle.

We report in Figure 3d the effects of temperature and pressure on the anisotropy of the tetragonal phase. Here, quantum fluctuations play a non-negligible role that cannot be accounted for with MD or static DFT calculations. In contrast with previous reports⁷, our simulations of the c/a tetragonal anisotropy show an excellent agreement with the X-ray diffraction data obtained in diamond-anvil cells⁵⁶, and highlight how pressure favors the tetragonal anisotropy, reflected in the positive slope of the phase-boundary with the cubic phase (Figure 2a).

B. Elastic properties and sound velocity

Geological models can be validated by analyzing seismic wave propagation through the lower mantle, which requires knowledge of the elastic properties of the materials that compose it. Unfortunately, CaSiO₃ is unquenchable at room conditions, and due to the difficulties in synthesizing samples sufficiently large to measure sound velocities, very few experimental data are available at high pressures. For this reason, first-principles simulations are crucial. However, recent works showed how state-of-the-art approaches fail to reproduce the experimental elastic properties at low pressures³⁷. In particular, static DFT systematically overestimates the shear

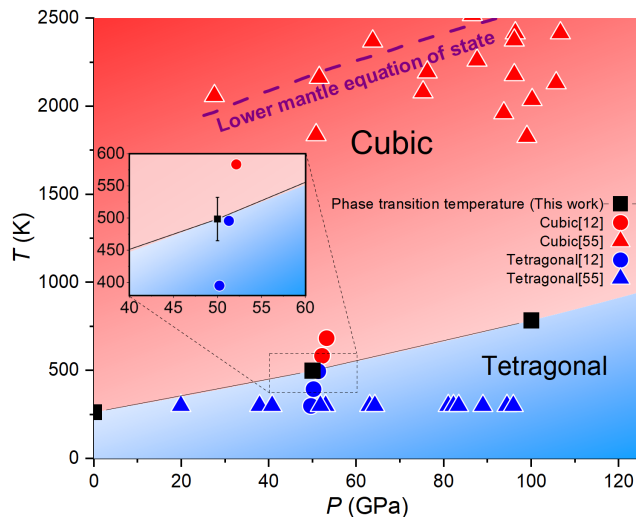


Figure 2: Pressure-temperature phase diagram of CaSiO_3 . The phase boundary evaluated in this work is reported with the black line. The error bar has been estimated from the stochastic sampling of the free energy at the transition temperature to be ~ 30 K. Experimental data^{12,55} are reported in red (blue) for the cubic (tetragonal) phase. The purple dashed line represents the lower mantle’s equation of state.

modulus^{7,57,58} and, consequently, the transverse wave speed, while FPMD simulations improve in agreement with experiments⁵⁹.

Two hypotheses were suggested to explain the low shear modulus of CaSiO_3 . The first assumes the stability of the tetragonal phase in the lower mantle^{7,8}, which we already disproved in the first part of this work. The second hypothesis asserts that shear favors a rotation of oxygen octahedra similar to the tetragonal distortion, thus hypothesizing that the propagation of the transverse sound wave occurs similarly between the cubic and the tetragonal phase^{59,60}. However, if a shear deformation of the cubic cell were to result in a rotation of oxygen octahedra, then the cubic phase would become unstable at high temperatures under a finite shear strain. In particular, at least one of the triple degenerate low-frequency phonon modes at R of the free energy Hessian, associated with the rotation of the oxygen octahedra, would become imaginary. To test this hypothesis, we calculated the free energy Hessian of a shear strained 5-atom cubic structure at 100 GPa and 3000 K (Figure 3c), and indeed the triple degenerate low-frequency mode at R becomes split by the shear (the presence of the shear introduces a favorite axis for the oxygen octahedral rotation). However, all three modes remain positive, with no sign of instability. Moreover, even the frequency of the lowest one increases under shear when compared to the cubic structure. This indicates that shear increases the free energy barrier to rotate the oxygen octahedra even at 3000 K, disproving the hypothesis that shear stabilizes octahedral tilts at high temperatures.

We evaluate the isothermal sound velocity from the

slope of the acoustic physical phonons at finite temperatures. For this purpose, we employ the phonons as obtained from the dispersion of the free energy Hessian, which coincides with the poles of the dynamical Green’s function (the actual physical excitations of the lattice in a strongly anharmonic material)^{46,61} in the $\omega \rightarrow 0$ limit. This condition is realized in the acoustic modes near Γ . The free energy Hessian accounts for a negative-semidefinite “bubble” diagram^{46,62} that reduces the slope of the acoustic phonons and is the real reason for the lower shear modulus at finite temperatures reported by FPMD compared to harmonic predictions⁵⁹. We reach a good agreement with experimental data for the longitudinal sound velocity (Figure 3b); the simulated transverse sound velocity (Figure 3a) agrees with predictions from FPMD and it improves the experimental agreement over static DFT calculations⁸, but it is still significantly overestimated. This is due to the simulations’ harder shear modulus value than experimental measurements. Therefore, the remaining possible explanation for the discrepancy is the limited precision of the exchange-correlation functional, here employed at the generalized-gradient approximation (GGA) within the PBEsol scheme⁴⁴.

C. Thermal transport

Mass transfer is impeded at the boundary separating the Earth’s core from the lower mantle; thus, the mechanism driving heat transport predominantly relies on thermal diffusion. Here, we report the lattice thermal conductivity of CaSiO_3 at the thermodynamic conditions of the lower mantle and investigate the role played by the anharmonicity of the crystal at high temperatures. A previous study investigated thermal transport of CaSiO_3 ⁴² employing the Boltzmann transport equation. In Figure 4d, we report the phonon spectra, including physical linewidth at 0 GPa and 1000 K, computed through the time-dependent self-consistent harmonic approximation^{61,62}. The overlap between the phonon spectra in the $300\text{-}600\text{ cm}^{-1}$ energy range highlights the possible tunneling between phonons at high temperatures. Moreover, while the phonon scattering rates are lower than their frequency, the phonon spectrum presents broad features and satellite peaks (Figure 4d), thus questioning the applicability of the Boltzmann transport theory and the need to explore the role played by coherent transport across different phonon bands. This can be investigated through the Wigner formulation of thermal transport^{17,43,63,64}, which accounts for both wave-like tunneling between different phonon modes and the standard particle-like (Peierls) propagation.

Since the anharmonic dressing of the phonons stabilizes the structure, providing positive-definite phonons, it allows us to employ the anharmonic renormalized phonon bands for calculating thermal transport in the cubic CaSiO_3 , which would be impossible within the standard per-

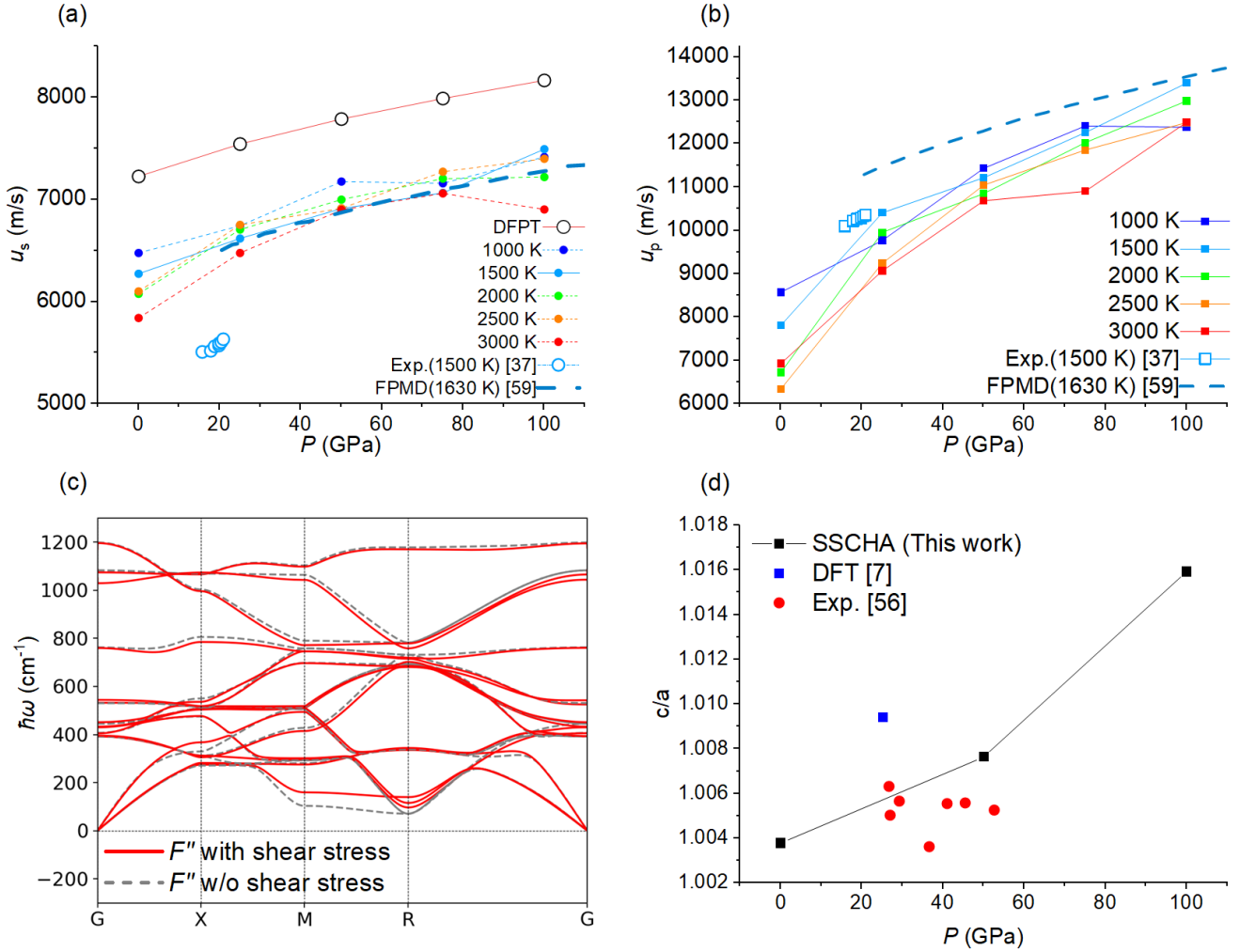


Figure 3: (a) Transverse sound velocity u_s and (b) longitudinal sound velocity u_p of CaSiO₃ at different pressures and temperatures. (c) The free energy Hessian $F'' = \frac{\partial^2 F}{\partial R_a \partial R_b}$ of CaSiO₃ under shear (at 100 GPa of surrounding pressure, 3000 K and shear of 0.01). The apparent presence of more phonon bands in the deformed structure is due to loss of degeneracy upon cubic symmetry breaking under shear. (d) Lattice parameters ratio (ratio of length of unit cell edges c and a) of the I4/mcm unit cell at 300 K.

turbation theory due to the imaginary harmonic phonon bands. In this way, we also account for the thermal effects that significantly harden M-R low-frequency bands and soften the high-energy breathing modes of oxygen.

The present results show that the Wigner diffusion of the heat wave of CaSiO₃ is suppressed by high pressure in the lower mantle. In contrast, it plays a major role at ambient pressure (Figure 4b). This can be understood in detail by looking at the distribution of phonon lifetimes (see SI. 3 in supplementary information): In the high pressure and low temperature regime (SI. 3d), these are mainly localized above the so-called Wigner limit, and so particle-like propagation dominates thermal transport⁴³. On the other hand, in the low pressure and high temperature regime (SI. 3a) the phonon lifetimes cloud lies on the Wigner limit and so wave-like effects become relevant⁴³.

In conclusion, our findings provide crucial insights into

the thermodynamics of CaSiO₃ under Earth's lower mantle conditions. We demonstrated that CaSiO₃ consistently exists in its cubic phase, with possible metastable tetragonal distortions observed above the transition temperature due to the identified first-order kind of phase transition. Notably, quantum fluctuations remain significant in the thermodynamics of this material, even at high temperatures, due to the strong covalent bonds that stiffen under pressure. Our results align well with available X-ray data and measurements of the longitudinal sound velocity, although they slightly overestimate the transverse sound velocity. Lastly, we presented the thermal conductivity of this material as a function of depth, highlighting that, despite the substantial anharmonicity of the phonon bands, its behavior is effectively captured by Boltzmann transport theory.

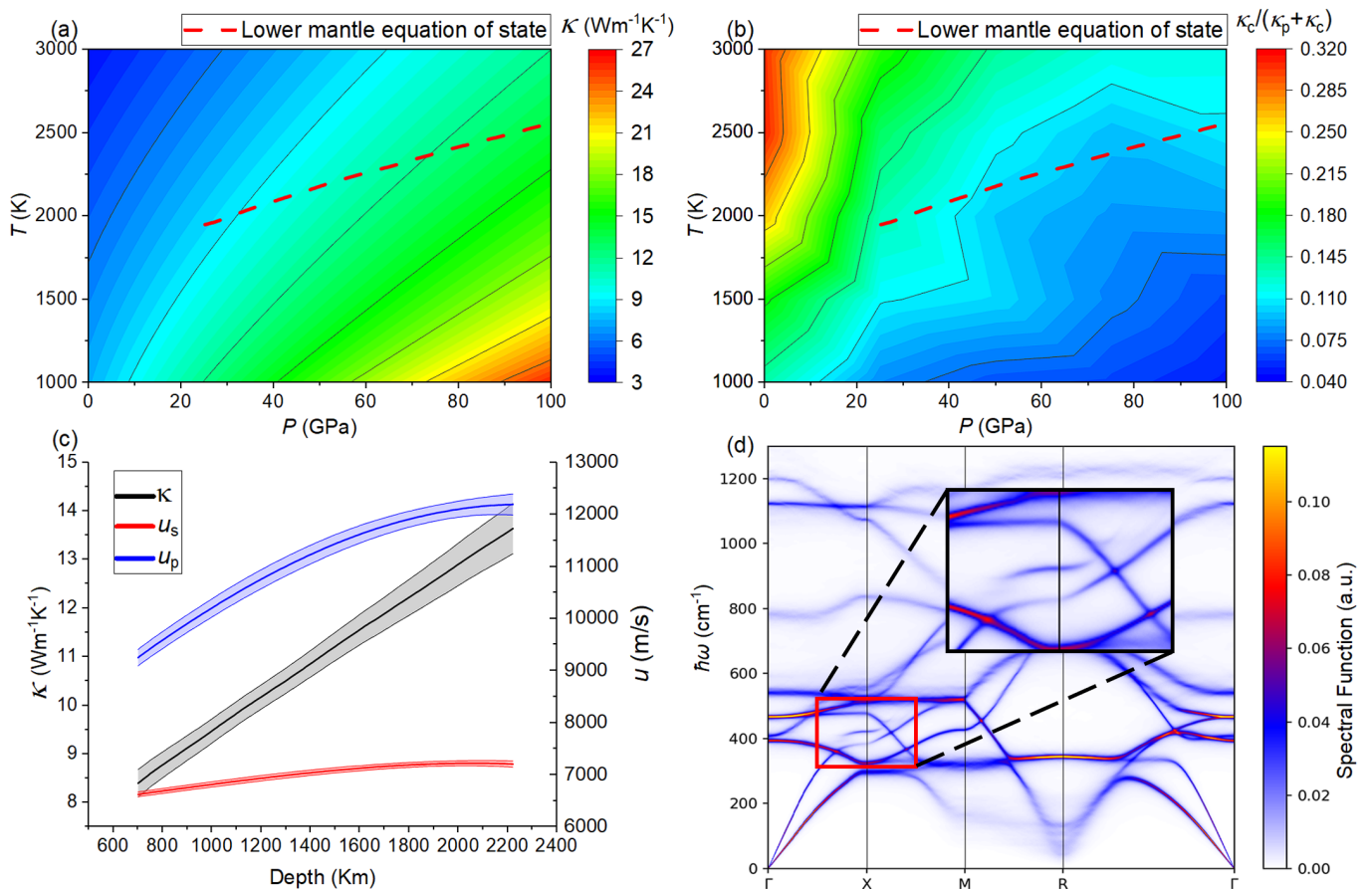


Figure 4: (a) Thermal conductivity of CaSiO₃ at different pressures and temperatures, (b) $\frac{\kappa_c}{\kappa_p+\kappa_c}$, where κ_p and κ_c are particle-like and wave-like contributions to the thermal conductivity. The purple dashed line represents the lower mantle's equation of state. (c) Thermal conductivity κ , transverse sound velocity u_s and longitudinal sound velocity u_p as a function of depth. (d) Spectral function of CaSiO₃ at 100 GPa and 2500 K. A small satellite band appears between 400 cm⁻¹ and 500 cm⁻¹ at symmetry point X (highlighted in the red box), showcasing the strong anharmonicity of CaSiO₃ even at very high pressure.

METHODS

The anharmonicity of CaSiO₃ is described through the stochastic self-consistent harmonic approximation (SSCHA)⁴⁸. A trial Gaussian density matrix for the nuclei is optimized to minimize the quantum free energy of the lattice. The trial Gaussian density matrix is parametrized through the average positions of atoms (centroids) and quantum-thermal nuclear fluctuations (covariance matrix)⁴⁹. The Gaussian constraint is the least possible biased choice: it is the distribution maximizing the entropy where centroids and covariance matrix are the only two parameters. A one-to-one mapping exists between a harmonic Hamiltonian and the corresponding Gaussian density matrix. This mapping allows for the direct entropy calculation of the trial density matrix. The SSCHA evaluates the quantum free energy as:

$$F \geq F[\bar{\rho}] = \langle K + V \rangle_{\bar{\rho}} - TS[\bar{\rho}], \quad (2)$$

where K is the kinetic energy, S is the entropy (both known analytically for any Gaussian density matrix), and $V(\mathbf{R})$ is the interatomic potential energy landscape. The average of Eq. (2) is computed with a Monte Carlo algorithm on randomly displaced ionic configurations described elsewhere⁴⁸. For each random configuration, $V(\mathbf{R})$ is evaluated as the ground state energy of density-functional theory (DFT) calculations within the Born-Oppenheimer approximation. The DFT calculations are solved in a plane-wave basis set as implemented in Quantum ESPRESSO⁶⁵ with the PBEsol⁴⁴ approximation for the exchange-correlation functional and a combination of ultrasoft and Projected Augmented Wave pseudopotentials from the SSSP library (precision version 1.3)⁶⁶. The plane-wave basis set is truncated using a cutoff of 80 Ry for wavefunction kinetic energy and 640 Ry for the charge density. We employed supercell calculation with 40 atoms for all phases (cubic, tetragonal, and cubic with a shear), sampling the Brillouin zone with a $2 \times 2 \times 2$ Monkhorst-Pack mesh.

To evaluate the volume and cell shape as a function

of both temperature and pressure, the lattice vectors are optimized to minimize the Gibbs free energy

$$G = F - P\Omega \quad (3)$$

where Ω is the volume of the primitive cell, and P is the target pressure⁴⁸. The SSCHA has already been applied successfully to a wide range of strongly anharmonic systems, as in high-pressure hydrogen and hydrides^{67–69}, low dimensional materials^{70,71}, and second-order phase transitions in perovskite structures similar to CaSiO_3 with unstable harmonic phonons^{53,72,73}.

The SSCHA allows us to rigorously compute the Free energy landscape as a function of the average nuclear position. Thanks to the Landau theory of phase transitions, this can be employed to study energy barriers between phases and second-order phase transitions by computing the curvature of the free energy landscape along the order parameter. The curvature change in the free energy landscape at the point where the order parameter is zero (the high-symmetry phase) identifies the critical point of a second-order phase transition. The SSCHA can compute the critical point for the tetragonal to cubic by evaluating the free energy Hessian⁴⁶:

$$\frac{\partial F}{\partial R_a \partial R_b} = \Phi_{ab} + \sum_{cdeflm} \Phi_{acd}^{(3)} [1 - \Lambda \Phi]_{cdef}^{-1} \Lambda_{eflm} \Phi_{lmb}^{(3)} \quad (4)$$

The sound velocity is evaluated with the static linear response theory at finite temperature within the *bubble* approximation⁴⁶, using Fourier interpolations to evaluate the response at small \mathbf{q} -points not commensurate with the original simulation cell⁷⁴. This allows us to determine precise sound velocities without requiring large supercells in molecular dynamics simulations. Since the simulation keeps the temperature fixed, perturbation theory computes the isothermal sound velocity. The fast vibration of seismic waves compared to the equilibration time requires the calculation of adiabatic sound velocity, which can be obtained with standard thermodynamic relations employing the computed bulk modulus and thermal expansion rate evaluated from the variable cell relaxation. The conversion between isentropic sound velocity and isothermal sound velocity is expressed as follows:

$$u_{s,S} = u_{s,T} \\ u_{p,S} = \sqrt{u_{p,T}^2 + \frac{B_S - B_T}{\rho}}, \quad (5)$$

where u_s and u_p represent transverse and longitudinal sound velocities, while B stands for bulk modulus, ρ is the density of the material, and S and T indexes indicate isentropic and isothermal conditions, respectively. The isentropic bulk modulus here is obtained by

$$\frac{1}{B_S} = \frac{1}{B_T} + \alpha_V \frac{\left(\frac{\partial S}{\partial P}\right)_T}{\left(\frac{\partial S}{\partial T}\right)_P}, \quad (6)$$

where α_V is the thermal expansion coefficient, and $\left(\frac{\partial S}{\partial P}\right)_T$ and $\left(\frac{\partial S}{\partial T}\right)_P$ are partial derivatives of entropy with respect to pressure and temperature.

The dynamical extension of SSCHA (time-dependent SSCHA)^{61,62,75,76} allows us to obtain interacting phonon Green functions describing lattice excitations. From the imaginary part of the phononic Green functions, we estimate the spectrum of phonons reported in Figure 4d. From the phonon spectral function, we derive phonon-quasiparticles' lifetimes to calculate the lattice thermal conductivity in a temperature range that includes the characteristic temperatures of the lower mantle. This is expressed following the Wigner formalism as^{17,43,77}.

$$\kappa_{tot}^{\alpha\beta} = \kappa_{P,SMA}^{\alpha\beta} + \frac{1}{(2\pi)^3} \int_{BZ} \sum_{s \neq s'} \frac{\omega(\mathbf{q})_s + \omega(\mathbf{q})_{s'}}{4} \\ \times \left[\frac{C(\mathbf{q})_s}{\omega(\mathbf{q})_s} + \frac{C(\mathbf{q})_{s'}}{\omega(\mathbf{q})_{s'}} \right] V^\alpha(\mathbf{q})_{s,s'} V^\beta(\mathbf{q})_{s',s} \\ \times \frac{\frac{1}{2}[\Gamma(\mathbf{q})_s + \Gamma(\mathbf{q})_{s'}]}{[\omega(\mathbf{q})_{s'} - \omega(\mathbf{q})_s]^2 + \frac{1}{4}[\Gamma(\mathbf{q})_s + \Gamma(\mathbf{q})_{s'}]^2} d^3q, \quad (7)$$

where $\kappa_{P,SMA}^{\alpha\beta}$ stands for the Peierls-Boltzmann (particle-like) conductivity, governed by phonon-phonon scattering within the single-mode relaxation time approximation (SMA). The additional term is the positive-definite tensor ($\kappa_C^{\alpha\beta}$) arising from the wave-tunneling between two non-degenerate bands ($s \neq s'$). For each wave vector \mathbf{q} , the $\omega(\mathbf{q})_s$ represents the frequency of the s -phonon mode. The specific heat $C(\mathbf{q}_s)$ is calculated with equilibrium Bose-Einstein distribution $\bar{N}(\mathbf{q})_s$ at temperature T , $V^\alpha(\mathbf{q})_{s,s'}$ and $V^\beta(\mathbf{q})_{s,s'}$ represents the cartesian components of the velocity operator whose diagonal elements ($s = s'$) give phonon group velocity. $\Gamma(\mathbf{q})_s$ are phonon linewidths. From the Lorentzian profile, it is clearly seen that when phonon linewidths are comparable to the interband energy spacing then wave-like heat conduction yields a non-negligible contribution to the overall thermal transport. On the contrary, when the opposite regime is verified thermal transport is mainly of particle-like nature. The calculation of thermal transport is performed within the Phono3py software¹⁸.

- ¹ T. Katsura, A. Yoneda, D. Yamazaki, T. Yoshino, and E. Ito, "Adiabatic temperature profile in the mantle," *Physics of the Earth and Planetary Interiors*, vol. 183, no. 1-2, pp. 212–218, 2010.
- ² A. M. Dziewonski and D. L. Anderson, "Preliminary reference earth model," *Physics of the earth and planetary interiors*, vol. 25, no. 4, pp. 297–356, 1981.
- ³ T. Gasparik, K. Wolf, and C. M. Smith, "Experimental determination of phase relations in the casio3 system from 8 to 15 gpa," *American Mineralogist*, vol. 79, no. 11-12, pp. 1219–1222, 1994.
- ⁴ G. Shen and P. Lazor, "Measurement of melting temperatures of some minerals under lower mantle pressures," *Journal of Geophysical Research: Solid Earth*, vol. 100, no. B9, pp. 17699–17713, 1995.
- ⁵ A. Zerr, G. Serghiou, and R. Boehler, "Melting of casio3 perovskite to 430 kbar and first in-situ measurements of lower mantle eutectic temperatures," *Geophysical research letters*, vol. 24, no. 8, pp. 909–912, 1997.
- ⁶ J. Braithwaite and L. Stixrude, "Melting of casio3 perovskite at high pressure," *Geophysical Research Letters*, vol. 46, no. 4, pp. 2037–2044, 2019.
- ⁷ L. Stixrude, C. Lithgow-Bertelloni, B. Kiefer, and P. Fumagalli, "Phase stability and shear softening in ca si o 3 perovskite at high pressure," *Physical Review B*, vol. 75, no. 2, p. 024108, 2007.
- ⁸ L. Li, D. J. Weidner, J. Brodholt, D. Alfe, G. D. Price, R. Caracas, and R. Wentzcovitch, "Phase stability of casio3 perovskite at high pressure and temperature: Insights from ab initio molecular dynamics," *Physics of the Earth and Planetary Interiors*, vol. 155, no. 3-4, pp. 260–268, 2006.
- ⁹ D. J. Adams and A. R. Oganov, "Ab initio molecular dynamics study of ca si o 3 perovskite at p- t conditions of earth's lower mantle," *Physical Review B*, vol. 73, no. 18, p. 184106, 2006.
- ¹⁰ A. Thomson, W. Crichton, J. Brodholt, I. Wood, N. Sierisch, J. Muir, D. Dobson, and S. A. Hunt, "Seismic velocities of casio3 perovskite can explain llsvps in earth's lower mantle," *Nature*, vol. 572, no. 7771, pp. 643–647, 2019.
- ¹¹ N. Sun, Z. Mao, S. Yan, X. Wu, V. B. Prakapenka, and J.-F. Lin, "Confirming a pyrolitic lower mantle using self-consistent pressure scales and new constraints on casio3 perovskite," *Journal of Geophysical Research: Solid Earth*, vol. 121, no. 7, pp. 4876–4894, 2016.
- ¹² T. Kurashina, K. Hirose, S. Ono, N. Sata, and Y. Ohishi, "Phase transition in al-bearing casio3 perovskite: implications for seismic discontinuities in the lower mantle," *Physics of the Earth and Planetary Interiors*, vol. 145, no. 1-4, pp. 67–74, 2004.
- ¹³ A. Ricolleau, J.-p. Perrillat, G. Fiquet, I. Daniel, J. Matas, A. Addad, N. Menguy, H. Cardon, M. Mezouar, and N. Guignot, "Phase relations and equation of state of a natural morb: Implications for the density profile of subducted oceanic crust in the earth's lower mantle," *Journal of Geophysical Research: Solid Earth*, vol. 115, no. B8, 2010.
- ¹⁴ J. Immoor, L. Miyagi, H.-P. Liermann, S. Speziale, K. Schulze, J. Buchen, A. Kurnosov, and H. Marquardt, "Weak cubic casio3 perovskite in the earth's mantle," *Nature*, vol. 603, no. 7900, pp. 276–279, 2022.
- ¹⁵ L. Miyagi, S. Merkel, T. Yagi, N. Sata, Y. Ohishi, and H.-R. Wenk, "Diamond anvil cell deformation of casio3 perovskite up to 49 gpa," *Physics of the Earth and Planetary Interiors*, vol. 174, no. 1-4, pp. 159–164, 2009.
- ¹⁶ S. R. Shieh, T. S. Duffy, and G. Shen, "Elasticity and strength of calcium silicate perovskite at lower mantle pressures," *Physics of the Earth and Planetary Interiors*, vol. 143, pp. 93–105, 2004.
- ¹⁷ M. Simoncelli, N. Marzari, and F. Mauri, "Unified theory of thermal transport in crystals and glasses," *Nature Physics*, vol. 15, no. 8, pp. 809–813, 2019.
- ¹⁸ A. Togo, L. Chaput, and I. Tanaka, "Distributions of phonon lifetimes in brillouin zones," *Phys. Rev. B*, vol. 91, p. 094306, Mar 2015.
- ¹⁹ W. Li, J. Carrete, N. A. Katcho, and N. Mingo, "ShengBTE: a solver of the Boltzmann transport equation for phonons," *Comp. Phys. Commun.*, vol. 185, p. 1747–1758, 2014.
- ²⁰ J. Carrete, B. Vermeersch, A. Katre, A. van Roekeghem, T. Wang, G. K. Madsen, and N. Mingo, "almabte: A solver of the space-time dependent boltzmann transport equation for phonons in structured materials," *Computer Physics Communications*, vol. 220, pp. 351–362, 2017.
- ²¹ M. Raya-Moreno, X. Cartoixa, and J. Carrete, "Bte-barna: An extension of almabte for thermal simulation of devices based on 2d materials," *Computer Physics Communications*, vol. 281, p. 108504, 2022.
- ²² Z. Ding, K. Chen, B. Song, J. Shin, A. A. Maznev, K. A. Nelson, and G. Chen, "Observation of second sound in graphite over 200 k," *Nature communications*, vol. 13, no. 1, p. 285, 2022.
- ²³ S. Huberman, R. A. Duncan, K. Chen, B. Song, V. Chiloyan, Z. Ding, A. A. Maznev, G. Chen, and K. A. Nelson, "Observation of second sound in graphite at temperatures above 100 k," *Science*, vol. 364, no. 6438, pp. 375–379, 2019.
- ²⁴ X. Huang, Y. Guo, Y. Wu, S. Masubuchi, K. Watanabe, T. Taniguchi, Z. Zhang, S. Volz, T. Machida, and M. Nomura, "Observation of phonon poiseuille flow in isotopically purified graphite ribbons," *Nature Communications*, vol. 14, no. 1, p. 2044, 2023.
- ²⁵ S. Lee, D. Broido, K. Esfarjani, and G. Chen, "Hydrodynamic phonon transport in suspended graphene," *Nature communications*, vol. 6, no. 1, p. 6290, 2015.
- ²⁶ A. Cepellotti and N. Marzari, "Boltzmann transport in nanostructures as a friction effect," *Nano letters*, vol. 17, no. 8, pp. 4675–4682, 2017.
- ²⁷ L. Sendra, A. Beardo, J. Bafaluy, P. Torres, F. X. Alvarez, and J. Camacho, "Hydrodynamic heat transport in dielectric crystals in the collective limit and the drifting/driftless velocity conundrum," *Physical Review B*, vol. 106, no. 15, p. 155301, 2022.
- ²⁸ J. Jeong, X. Li, S. Lee, L. Shi, and Y. Wang, "Transient hydrodynamic lattice cooling by picosecond laser irradiation of graphite," *Physical Review Letters*, vol. 127, no. 8, p. 085901, 2021.
- ²⁹ L. Restuccia and D. Jou, "Non-local vectorial internal variables and generalized guyer-krumhansl evolution equations for the heat flux," *Entropy*, vol. 25, no. 9, p. 1259, 2023.
- ³⁰ M. Sýkora, M. Pavelka, L. Restuccia, and D. Jou, "Multiscale heat transport with inertia and thermal vortices,"

- Physica Scripta*, vol. 98, no. 10, p. 105234, 2023.
- 31 E. Di Lucente, F. Libbi, and N. Marzari, “Vorticity and compressibility hydrodynamics in electron and phonon fluids,” *Bulletin of the American Physical Society*, 2024.
 - 32 L. Ponet, E. Di Lucente, and N. Marzari, “The energy landscape of magnetic materials,” *npj Computational Materials*, vol. 10, no. 1, p. 151, 2024.
 - 33 T. Lay, J. Hernlund, and B. A. Buffett, “Core–mantle boundary heat flow,” *Nature Geoscience*, vol. 1, pp. 25–32, Jan. 2008.
 - 34 D. Alfe, M. Gillan, and G. Price, “The melting curve of iron at the pressures of the earth’s core from ab initio calculations,” *Nature*, vol. 401, no. 6752, pp. 462–464, 1999.
 - 35 D. Sagatova, A. Shatskiy, N. Sagatov, and K. Litasov, “Phase relations in casio 3 system up to 100 gpa and 2500 k,” *Geochemistry International*, vol. 59, pp. 791–800, 2021.
 - 36 T. S. Sokolova and P. I. Dorogokupets, “Equations of state of ca-silicates and phase diagram of the casio3 system under upper mantle conditions,” *Minerals*, vol. 11, no. 3, p. 322, 2021.
 - 37 S. Gréaux, T. Irifune, Y. Higo, Y. Tange, T. Arimoto, Z. Liu, and A. Yamada, “Sound velocity of casio3 perovskite suggests the presence of basaltic crust in the earth’s lower mantle,” *Nature*, vol. 565, no. 7738, pp. 218–221, 2019.
 - 38 A. Hofmeister, *Heat transport and energetics of the earth and rocky planets*. Elsevier, 2019.
 - 39 K. Lodders and B. Fegley, *The planetary scientist’s companion*. Oxford University Press on Demand, 1998.
 - 40 G. Schubert, *Treatise on geophysics*. Elsevier, 2015.
 - 41 S. Rost, “Core–mantle boundary landscapes,” *Nature Geoscience*, vol. 6, no. 2, pp. 89–90, 2013.
 - 42 Z. Zhang, D.-B. Zhang, K. Onga, A. Hasegawa, K. Ohta, K. Hirose, and R. M. Wentzcovitch, “Thermal conductivity of casio 3 perovskite at lower mantle conditions,” *Physical Review B*, vol. 104, no. 18, p. 184101, 2021.
 - 43 E. Di Lucente, M. Simoncelli, and N. Marzari, “Crossover from boltzmann to wigner thermal transport in thermoelectric skutterudites,” *Phys. Rev. Res.*, vol. 5, p. 033125, Aug 2023.
 - 44 J. P. Perdew, A. Ruzsinszky, G. I. Csonka, O. A. Vydrov, G. E. Scuseria, L. A. Constantin, X. Zhou, and K. Burke, “Restoring the density-gradient expansion for exchange in solids and surfaces,” *Physical Review Letters*, vol. 100, no. 13, p. 136406.
 - 45 I. Errea, M. Calandra, and F. Mauri, “Anharmonic free energies and phonon dispersions from the stochastic self-consistent harmonic approximation: Application to platinum and palladium hydrides,” *Physical Review B*, vol. 89, no. 6, p. 064302, 2014.
 - 46 R. Bianco, I. Errea, L. Paulatto, M. Calandra, and F. Mauri, “Second-order structural phase transitions, free energy curvature, and temperature-dependent anharmonic phonons in the self-consistent harmonic approximation: Theory and stochastic implementation,” *Physical Review B*, vol. 96, no. 1, p. 014111, 2017.
 - 47 L. Monacelli, I. Errea, M. Calandra, and F. Mauri, “Pressure and stress tensor of complex anharmonic crystals within the stochastic self-consistent harmonic approximation,” *Phys. Rev. B*, vol. 98, p. 024106, Jul 2018.
 - 48 L. Monacelli, R. Bianco, M. Cherubini, M. Calandra, I. Errea, and F. Mauri, “The stochastic self-consistent harmonic approximation: calculating vibrational properties of materials with full quantum and anharmonic effects,” *Journal of Physics: Condensed Matter*, vol. 33, no. 36, p. 363001, 2021.
 - 49 L. Monacelli, “Simulating anharmonic crystals: Lights and shadows of first-principles approaches,” *arXiv preprint arXiv:2407.03090*, 2024.
 - 50 M. Miotto and L. Monacelli, “Fast prediction of anharmonic vibrational spectra for complex organic molecules,” *npj Computational Materials*, vol. 10, Oct. 2024.
 - 51 M. Paściak, T. Welberry, J. Kulda, S. Leoni, and J. Hlinka, “Dynamic displacement disorder of cubic batio 3,” *Physical review letters*, vol. 120, no. 16, p. 167601, 2018.
 - 52 L. Gigli, M. Veit, M. Kotiuga, G. Pizzi, N. Marzari, and M. Ceriotti, “Thermodynamics and dielectric response of BaTiO3 by data-driven modeling,” *npj Computational Materials*, vol. 8, p. 209, Sept. 2022.
 - 53 L. Monacelli and N. Marzari, “First-principles thermodynamics of CsSnI₃,” *Chemistry of Materials*, vol. 35, pp. 1702–1709, Feb. 2023.
 - 54 M. Kotiuga, S. Halilov, B. Kozinsky, M. Fornari, N. Marzari, and G. Pizzi, “Microscopic picture of paraelectric perovskites from structural prototypes,” *Physical Review Research*, vol. 4, no. 1, p. L012042, 2022.
 - 55 S. Ono, Y. Ohishi, and K. Mibe, “Phase transition of ca-perovskite and stability of al-bearing mg-perovskite in the lower mantle,” *American Mineralogist*, vol. 89, no. 10, pp. 1480–1485, 2004.
 - 56 H. Chen, S.-H. Shim, K. Leinenweber, V. Prakapenka, Y. Meng, and C. Prescher, “Crystal structure of casio3 perovskite at 28–62 gpa and 300 k under quasi-hydrostatic stress conditions,” *American Mineralogist: Journal of Earth and Planetary Materials*, vol. 103, no. 3, pp. 462–468, 2018.
 - 57 B. B. Karki and J. Crain, “Structure and elasticity of CaO at high pressure,” vol. 103, pp. 12405–12411.
 - 58 B. B. Karki, L. Stixrude, and R. M. Wentzcovitch, “High-pressure elastic properties of major materials of earth’s mantle from first principles,” vol. 39, no. 4, pp. 507–534.
 - 59 K. Kawai and T. Tsuchiya, “Small shear modulus of cubic casio3 perovskite,” *Geophysical Research Letters*, vol. 42, no. 8, pp. 2718–2726, 2015.
 - 60 R. Caracas, R. Wentzcovitch, G. D. Price, and J. Brodholt, “Casio3 perovskite at lower mantle pressures,” *Geophysical Research Letters*, vol. 32, no. 6, 2005.
 - 61 L. Monacelli and F. Mauri, “Time-dependent self-consistent harmonic approximation: Anharmonic nuclear quantum dynamics and time correlation functions,” *Physical Review B*, vol. 103, no. 10, p. 104305, 2021.
 - 62 A. Siciliano, L. Monacelli, G. Caldarelli, and F. Mauri, “Wigner gaussian dynamics: Simulating the anharmonic and quantum ionic motion,” *Phys. Rev. B*, vol. 107, p. 174307, May 2023.
 - 63 J. Klarbring, O. Hellman, I. A. Abrikosov, and S. I. Simak, “Anharmonicity and ultralow thermal conductivity in lead-free halide double perovskites,” *Physical Review Letters*, vol. 125, no. 4, p. 045701, 2020.
 - 64 G. Caldarelli, M. Simoncelli, N. Marzari, F. Mauri, and L. Benfatto, “Many-body green’s function approach to lattice thermal transport,” *Phys. Rev. B*, vol. 106, p. 024312, Jul 2022.
 - 65 P. Giannozzi, O. Andreussi, T. Brumme, O. Bunau, M. Buongiorno Nardelli, M. Calandra, R. Car, C. Cavazzoni, D. Ceresoli, M. Cococcioni, N. Colonna, I. Carnimeo, A. Dal Corso, S. de Gironcoli, P. Delugas, R. A. DiStasio, A. Ferretti, A. Floris, G. Fratesi, G. Fugallo, R. Gebauer,

- U. Gerstmann, F. Giustino, T. Gorni, J. Jia, M. Kawamura, H.-Y. Ko, A. Kokalj, E. Küçükbenli, M. Lazzeri, M. Marsili, N. Marzari, F. Mauri, N. L. Nguyen, H.-V. Nguyen, A. Otero-de-la Roza, L. Paulatto, S. Poncé, D. Rocca, R. Sabatini, B. Santra, M. Schlipf, A. P. Seitsonen, A. Smogunov, I. Timrov, T. Thonhauser, P. Umari, N. Vast, X. Wu, and S. Baroni, “Advanced capabilities for materials modelling with quantum espresso,” *Journal of Physics: Condensed Matter*, vol. 29, p. 465901, Oct. 2017.
- ⁶⁶ K. Lejaeghere, G. Bihlmayer, T. Björkman, P. Blaha, S. Blügel, V. Blum, D. Caliste, I. E. Castelli, S. J. Clark, A. Dal Corso, *et al.*, “Reproducibility in density functional theory calculations of solids,” *Science*, vol. 351, no. 6280, p. 1415, 2016.
- ⁶⁷ I. Errea, F. Belli, L. Monacelli, A. Sanna, T. Koretsune, T. Tadano, R. Bianco, M. Calandra, R. Arita, F. Mauri, and J. A. Flores-Livas, “Quantum crystal structure in the 250-kelvin superconducting lanthanum hydride,” *Nature*, vol. 578, pp. 66–69, Feb. 2020.
- ⁶⁸ L. Monacelli, M. Casula, K. Nakano, S. Sorella, and F. Mauri, “Quantum phase diagram of high-pressure hydrogen,” *Nature Physics*, p. 845, Mar. 2023.
- ⁶⁹ L. Monacelli, I. Errea, M. Calandra, and F. Mauri, “Black metal hydrogen above 360 GPa driven by proton quantum fluctuations,” *Nature Physics*, vol. 17, pp. 63–67, Sept. 2020.
- ⁷⁰ U. Aseginolaza, J. Diego, T. Cea, R. Bianco, L. Monacelli, F. Libbi, M. Calandra, A. Bergara, F. Mauri, and I. Errea, “Bending rigidity, sound propagation and ripples in flat graphene,” *Nature Physics*, vol. 20, p. 1288–1293, May 2024.
- ⁷¹ D. Romanin, L. Monacelli, R. Bianco, I. Errea, F. Mauri, and M. Calandra, “Dominant role of quantum anharmonicity in the stability and optical properties of infinite linear acetylenic carbon chains,” *The Journal of Physical Chemistry Letters*, vol. 12, p. 10339–10345, Oct. 2021.
- ⁷² L. Ranalli, C. Verdi, L. Monacelli, G. Kresse, M. Calandra, and C. Franchini, “Temperature-dependent anharmonic phonons in quantum paraelectric KTaO_3 by first principles and machine-learned force fields,” *Advanced Quantum Technologies*, vol. 6, p. 2200131, Feb. 2023.
- ⁷³ C. Verdi, L. Ranalli, C. Franchini, and G. Kresse, “Quantum paraelectricity and structural phase transitions in strontium titanate beyond density functional theory,” *Physical Review Materials*, vol. 7, Mar. 2023.
- ⁷⁴ R. Bianco, I. Errea, M. Calandra, and F. Mauri, “High-pressure phase diagram of hydrogen and deuterium sulfides from first principles: Structural and vibrational properties including quantum and anharmonic effects,” *Phys. Rev. B*, vol. 97, p. 214101, Jun 2018.
- ⁷⁵ F. Libbi, A. Johansson, L. Monacelli, and B. Kozinsky, “Atomistic simulations of out-of-equilibrium quantum nuclear dynamics,” *arXiv preprint arXiv:2408.00902*, 2024.
- ⁷⁶ F. Libbi, A. Johansson, B. Kozinsky, and L. Monacelli, “Ultrafast quantum dynamics in SrTiO_3 under impulsive thz radiation,” *arXiv preprint arXiv:2408.12421*, 2024.
- ⁷⁷ M. Simoncelli, N. Marzari, and F. Mauri, “Wigner formulation of thermal transport in solids,” *Physical Review X*, vol. 12, no. 4, p. 041011, 2022.

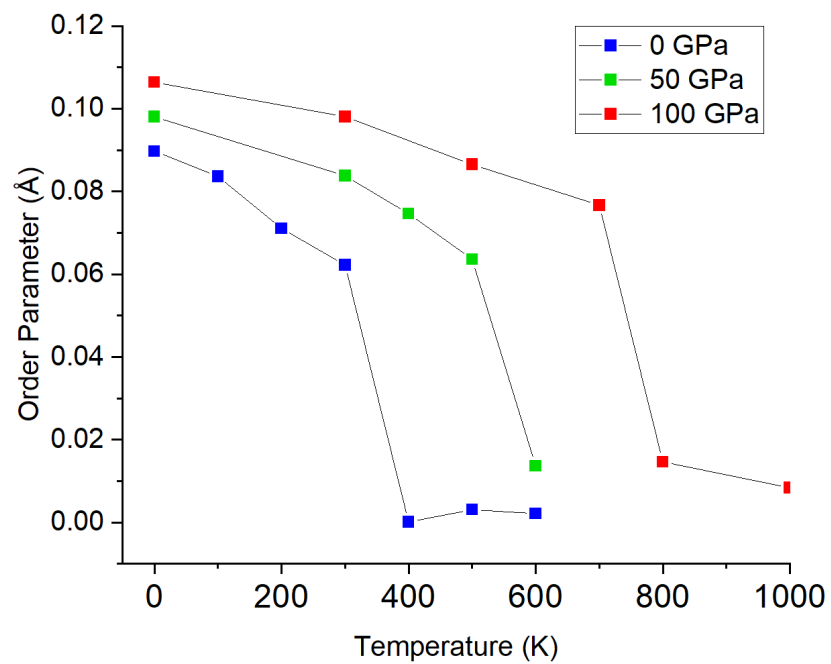
**The thermodynamics of CaSiO₃ in Earth's lower mantle:
supplementary information**

Yongjoong Shin,¹ Enrico Di Lucente,¹ Nicola Marzari,^{1,2} and Lorenzo Monacelli^{3,1}

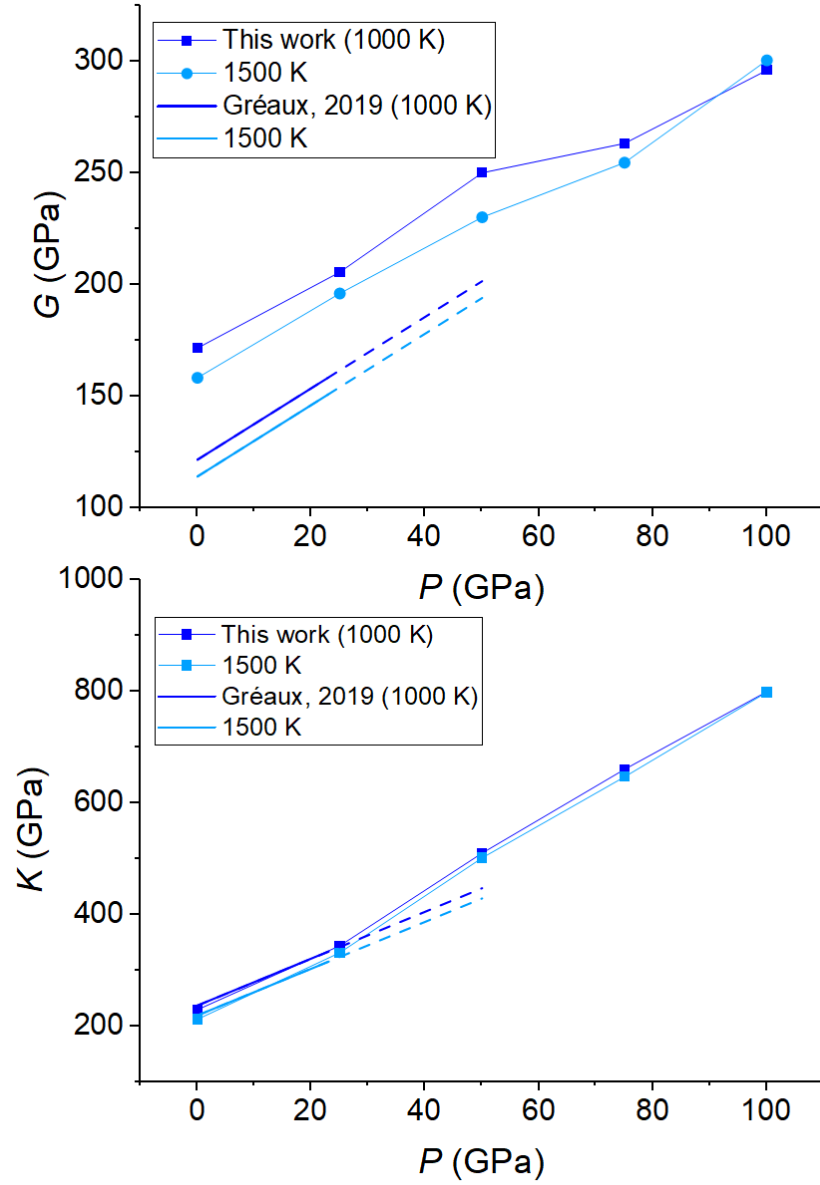
*¹Theory and Simulation of Materials (THEOS) and National Centre for
Computational Design and Discovery of Novel Materials (MARVEL),
École Polytechnique Fédérale de Lausanne, Lausanne 1015, Switzerland*

*²Laboratory for Materials Simulations,
Paul Scherrer Institut, 5232 Villigen PSI, Switzerland*

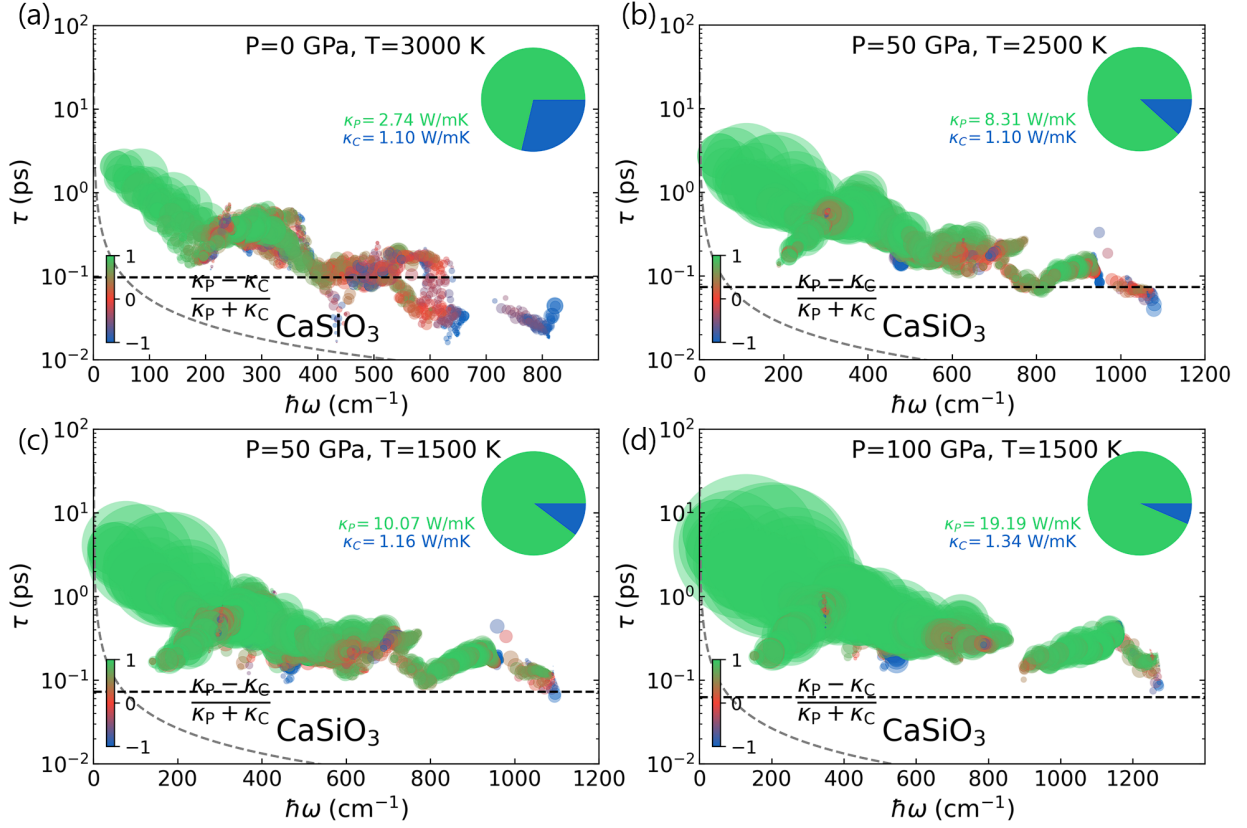
³Dipartimento di Fisica, Università di Roma La Sapienza, 00185 Roma, Italy



SI. 1: Order parameter as a function of temperature at 0, 50, 100 GPa



SI. 2: (a) Shear modulus G and (b) bulk modulus K obtained from SSCHA (this work) and shear and bulk modulus-pressure relation estimated from experiment results⁷. Comparing our results of shear modulus with experimental results, we find higher estimates than actual values. At 25 GPa and 1000 K, the shear modulus from experiments is 25 GPa, which is about 26% less than our predictions.



SI. 3: Distribution of phonon lifetimes as a function of energy for different temperatures and pressures. The Wigner limit in time (dashed horizontal line) corresponds to a phonon lifetime equal to the inverse of the average interband spacing ($\tau^\omega = \Delta\omega_{avg}^{-1}$), and the dashed hyperbola shows the Ioffe-Regel limit in time ($\tau^{IR} = \omega^{-1}$). The area of each scatter point is proportional to the contribution to the lattice thermal conductivity, and its color represent the origin of the contribution: $c = [\kappa_p - \kappa_c]/[\kappa_p + \kappa_c]$, where particle like is green and wavelike is blue.